J. Mech. Phys. Solids 198 (2025) 106064

Contents lists available at ScienceDirect

Journal of the Mechanics and Physics of Solids

journal homepage: www.elsevier.com/locate/jmps

Torsion-mediated instabilities in confined elastic layers

Tara K. Venkatadri [a,b,1], Chuwei Ye [c,1], Tal Cohen [d,e,*], Shaoting Lin [c,*]

[a] Department of Aeronautics and Astronautics, Massachusetts Institute of Technology, Cambridge, MA, 02139, USA
[b] Graduate Aerospace Laboratories, California Institute of Technology, Pasadena, CA, 91125, USA
[c] Department of Mechanical Engineering, Michigan State University, East Lansing, MI, 48824, USA
[d] Department of Civil and Environmental Engineering, Massachusetts Institute of Technology, Cambridge, MA, 02139, USA
[e] Department of Mechanical Engineering, Massachusetts Institute of Technology, Cambridge, MA, 02139, USA

ARTICLE INFO

Keywords:
Confined elastic layers
Instability
Torsion

ABSTRACT

When a soft elastic layer confined between two rigid substrates is subjected to tensile loads, the stressed layer exhibits various modes of elastic instability that influence its mechanical response. While previous studies have primarily focused on analyzing these instabilities under normal tension, this study systematically investigates the impact of combined tension–torsion loading on the emergence of fingering and fringe instabilities. Through a combination of theoretical, experimental, and numerical analysis, we show that the application of torsion can tune the mode of instabilities in elastic layers with moderate aspect ratios. We also demonstrate that torsion controls the monotonicity of the stress–stretch relationship in elastic layers with large aspect ratios. We construct a phase diagram that delineates the mode of instability and the monotonicity of the stress–stretch curve in confined elastic layers as a function of the applied torsion angle and the sample's aspect ratio. This work not only provides mechanistic insights into the role of torsion in stabilizing the response of confined elastic layers, but also offers a valuable tool for designing soft yet tough adhesive systems capable of withstanding complex mechanical loads.

1. Introduction

Layers of soft elastic materials confined between two rigid substrates are prevalent in nature. Examples include shellfish adhering to undersea rocks (Waite et al., 2005), barnacles attaching to ship decks (Vaccaro and Waite, 2001; Sun et al., 2004), and tendons connecting bones (Benjamin et al., 2006; Desmond et al., 2015). Beyond their natural occurrences, confined elastic layers are widely used in various engineering fields, with examples such as adhesives for tissues (Söntjens et al., 2006; Wang et al., 2022; Cui et al., 2020), joints for structures (Her and Chan, 2019; Osipov and Vermeir, 1996; Craik and Osipov, 1995), and coatings for materials (Liu et al., 2021; Khutoryanskaya et al., 2010; Kaniewska et al., 2020). Recently, to harness the full potential of these confined elastic layers in medicine, robotics, and electronics, various hydrogel adhesives have been developed, achieving high interfacial toughness when adhered to a range of engineering substrates including glass, metals, and ceramics (Yuk et al., 2016; Bovone et al., 2021; Feng et al., 2022). Such novel adhesives can undergo large elastic deformations before failure, and thus reveal new instabilities that are not well understood.

When a soft elastic layer confined between two rigid substrates is subjected to tensile loading, the stressed layer exhibits various modes of instability that influence the layer's mechanical response. For example, if the interface between the layer and the substrate

* Corresponding authors.
E-mail addresses: talco@mit.edu (T. Cohen), linshaot@msu.edu (S. Lin).
[1] These authors contributed equally to this work.

https://doi.org/10.1016/j.jmps.2025.106064
Received 17 October 2024; Received in revised form 17 December 2024; Accepted 30 January 2025
Available online 7 February 2025
0022-5096/© 2025 Elsevier Ltd. All rights are reserved, including those for text and data mining, AI training, and similar technologies.

is weak, the confined layer may partially detach from the substrate, leading to interface undulation (Chakrabarti and Chaudhury, 2013; Chaudhury et al., 2015), which can trigger adhesive failure of confined elastic layers. If the interface between the layer and the substrate is strong, the initially axially-symmetric deformation can become geometrically unstable, leading to the formation of circumferential undulations that are referred to as *fingering instability* (Biggins et al., 2013; Lin et al., 2017) if it initiates at the middle section of the layer, or as *fringe instability* (Lin et al., 2016) if it initiates near the confined fringes of the layer. Depending on the mode of instability, the layer may exhibit monotonic or nonmonotonic stress versus stretch relationships. Notably, the initiation and growth of both fingering and fringe instabilities are typically elastically reversible.

In practical applications, soft elastic layers confined between two rigid substrates are often subjected to torsion. For example, tissue adhesives and structural joints in real-world settings inevitably experience torsion due to complex loading conditions. In experimental characterizations, torsion is sometimes preferred over tension due to its ability to produce homogeneous shear deformation with examples such as rheology (Wang et al., 2011). Additionally, since the shear deformation caused by torsion is isochoric, torsion represents an ideal load for studying the viscoelasticity of hydrogels without the influences of poroelasticity (Hu and Suo, 2012).

Studies on the impact of torsion on soft elastic cylinders capable of undergoing large deformations have primarily focused on the Poynting effect (Small et al., 2024; Kanner and Horgan, 2008), surface delamination (Venkatadri et al., 2023), and adhesive strength (Wang and Kornfield, 2012; Chateauminois et al., 2010) of confined elastic layers. In addition, previous studies show that torsion can also induce elastic instabilities in confined elastic layers. For example, elastic layers with a large aspect ratio (such as long cylindrical rods) exhibit a twisting instability, evolving from an initial kink to a knot (Gent and Hua, 2004). Conversely, elastic layers with a small aspect ratio display a wrinkling instability on their lateral surface (Ciarletta and Destrade, 2014). Despite these studies, the impacts of torsion on fringe and fingering instabilities in confined elastic layers have not been studied to date.

In this work, we focus on cylindrical confined layers of various aspect ratios, investigating how the simultaneous application of tension and torsion influences fingering and fringe instabilities. Through a combination of theoretical, experimental, and numerical analyses, we demonstrate that applying torsion can tune the mode of instability in elastic layers with moderate aspect ratios. Additionally, torsion modulates the fingering behavior by controlling the monotonicity of the stress–stretch relationship in elastic layers with large aspect ratios. We further construct a phase diagram delineating the mode of instability and the monotonicity of the stress–stretch curve in confined elastic layers as a function of torsion angle and aspect ratio. This work not only provides mechanistic insights into the role of torsion in stabilizing the response of confined elastic layers, but also offers a valuable tool for designing soft yet tough adhesive systems capable of withstanding complex mechanical loads.

The paper is structured as follows: Section 2 defines the dimensionless parameters that govern the key features of the instability in this study. Sections 3 and 4 discuss the setup and results for the experiments and simulations, respectively. Section 5 presents the derivation of the theoretical framework. Section 6 compares the experimental and theoretical results, with particular emphasis on the effect of torsion on the monotonicity of the stress–stretch curves. In Section 7, a phase diagram is constructed to characterize the mode of mechanical instabilities and the monotonicity of the stress–stretch curve in confined elastic layers with various aspect ratios and torsion angles. Finally, Section 8 concludes the paper.

2. Physical and dimensionless parameters

As illustrated in Fig. 1, we consider cylindrical elastic layers with diameter D and height H in the undeformed (reference) state. The radius of the sample in the undeformed state is $R_0 = D/2$, and the aspect ratio is defined as R_0/H. The cylindrical elastic layer in the undeformed state occupies a region

$$0 \le R \le R_0, \qquad 0 \le \Theta \le 2\pi, \qquad -H/2 \le Z \le H/2 \tag{1}$$

The elastic layer is perfectly adhered to two rigid plates. The elastic layer is deformed by controlling the vertical and rotational motion of one plate, while the other remains stationary. The vertical motion controls the current height h and induces a tensile force F; meanwhile, the rotation controls the torsion angle α and induces a torque T. We define the applied nominal stress as $S = F/\pi R_0^2$, and the applied stretch as $\lambda = h/H$. At the onset of instability, the applied nominal stress and stretch reach a critical value, denoted by S_c and λ_c, respectively. The nominal stress can be normalized by the shear modulus μ of the elastic layers, which was extracted from the measured stress versus stretch curves in an experiment, as described in Appendix A.

3. Experimental setup and results

We developed a customized experimental setup to characterize the mode of instability and monotonicity of the stress–stretch curve in confined hydrogel layers subjected to controlled tension and torsion (Ye and Lin, 2024). As schematically illustrated in Fig. 2, the setup integrates a mechanical system for applying tension and torsion loads to hydrogel layers sandwiched between functionalized glass substrates, and an imaging system to capture their deformation and instabilities. Details of the hydrogel fabrication are given in Appendix B. The hydrogel's radius R_0 varied from 12 to 18 mm, and its thickness H was set as 3 mm, resulting in an aspect ratio R_0/H ranging from 4 to 6. During a typical test, the bottom glass substrate was fixed, while the top glass substrate was first rotated to a specified angle α at a twisting rate of 5 degree/s, and then stretched to a specified height h at a stretching rate of 0.5 mm/s. The applied force F was recorded by a load cell (LFT-25-1KG), and the deformation of the hydrogel layer (top and side views) was captured by cameras. The nominal stress was calculated as $S = F/(\pi R_0^2)$, while the applied stretch

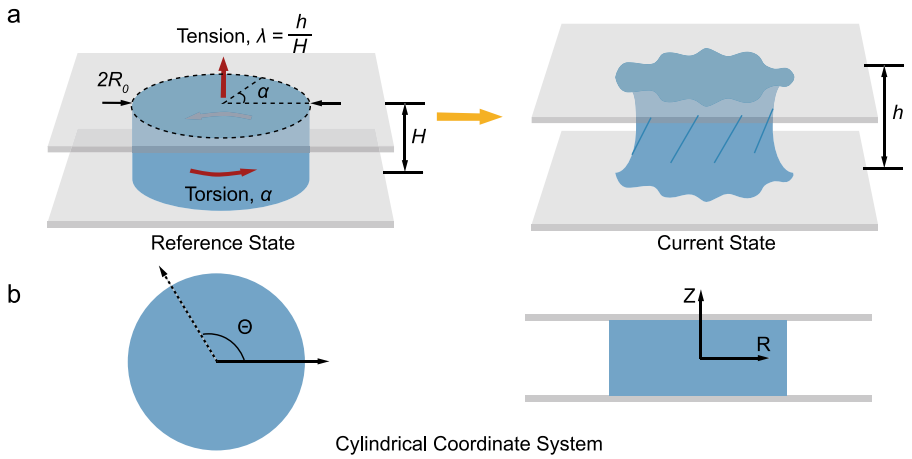


Fig. 1. Schematics of deformation and instabilities in confined elastic layers under tension and torsion. (a) The cylindrical confined elastic layer between two glass slides, subjected to tension and torsion, shown in the reference and current states. (b) The cylindrical coordinate system in the reference state.

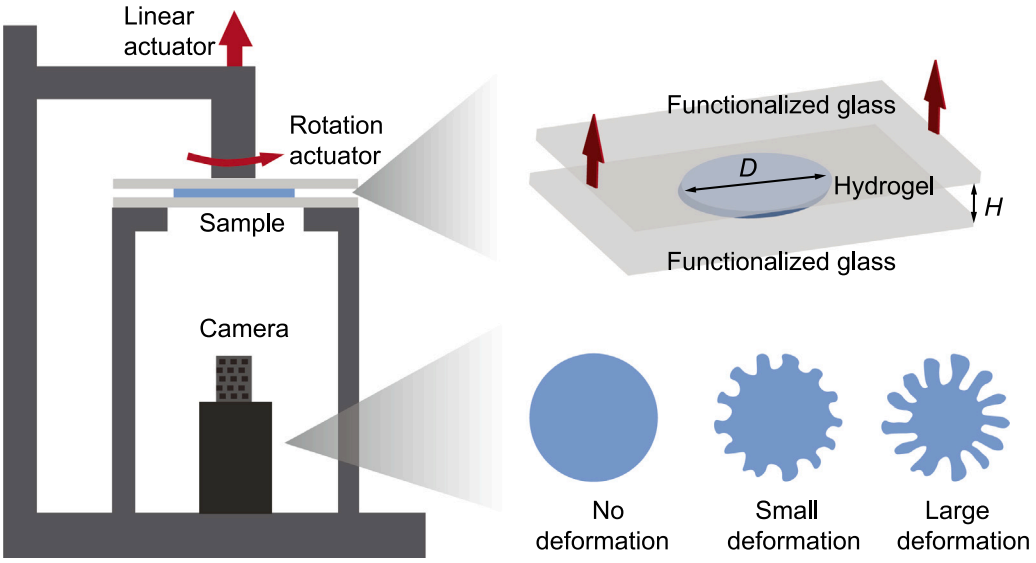


Fig. 2. Schematic illustration of the experimental setup. The setup integrates a mechanical system for applying controlled tension and torsion loads to hydrogel layers sandwiched between functionalized glass substrates, and an imaging system to capture their deformation and instabilities.

was identified by $\lambda = h/H$.

To examine the role of torsion, we first characterized the mechanical response of two hydrogel layers with an identical aspect ratio of $R_0/H = 4.8$: one without torsion ($\alpha = 0°$) and the other with torsion ($\alpha = 40°$). We measured their nominal stress versus stretch (S vs. λ) curves under tension, while simultaneously recording the initiation and development of elastic instabilities from both top and side views. For the hydrogel layer without torsion, the stress increases accordingly as the hydrogel layer is subjected to tension (Fig. 3a). At a critical stretch of $\lambda_c = 1.5$, the lateral surface of the hydrogel layer begins to undulate (Fig. 3b), initiating a fingering instability. As the stretch continues to increase, the layer displays a non-monotonic stress–stretch relationship peaking at an approximate stretch of 1.7, which indicates an unstable first-order transition of the fingering instability. Beyond this peak, as the stretch further increases, some of the developing fingers continue to grow, while others are suppressed. For the hydrogel layer with torsion, the initiation and development of the fingering patterns under tension are similar to the hydrogel layer without torsion (Fig. 3d). Interestingly, the hydrogel layer with torsion exhibits a monotonic stress–stretch relationship (Fig. 3c), suggesting that torsion plays a role in stabilizing the fingering process. Additionally, a negative stress is observed at $\lambda = 1$ for the hydrogel layer with torsion, which is attributed to the Poynting effect (Kanner and Horgan, 2008).

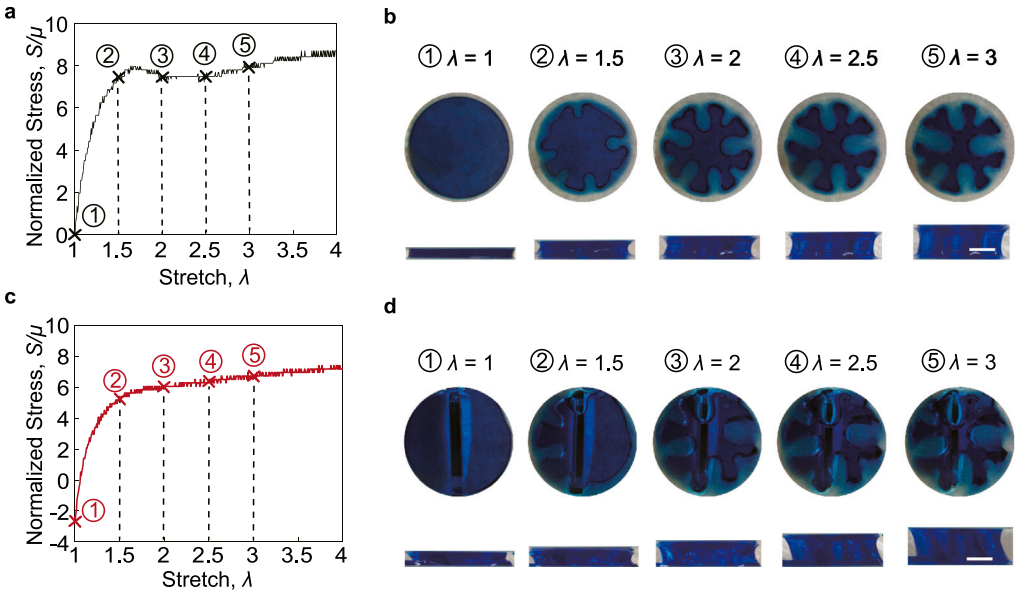


Fig. 3. Comparison between experimentally-observed mechanical responses of hydrogel layers ($R_0/H = 4.8$) with and without torsion. (a) Normalized nominal stress S/μ versus stretch λ of the hydrogel layer without torsion ($\alpha = 0°$) under tension. (b) Top and side views of the initiation and development of fingering patterns in the hydrogel layer without torsion ($\alpha = 0°$) at various stretches. (c) Normalized nominal stress S/μ versus stretch λ of the hydrogel layer with torsion ($\alpha = 40°$) under tension. (d) Top and side views of the initiation and development of fingering patterns in the hydrogel layer with torsion ($\alpha = 40°$) at various stretches. The scale bars in (b) and (d) are 5 mm.

4. Numerical simulation

We performed finite element simulations using ABAQUS/Explicit to capture the deformation and instability of elastic layers with various aspect ratios subjected to controlled tension and torsion. To focus on purely elastic behavior over a relatively short time scale, we modeled the hydrogel as a neo-Hookean material, neglecting water diffusion. We set the ratio between bulk modulus and shear modulus as 1000 to capture the incompressibility of the material. The element type was chosen as C3D8R, and the mesh size was set as 1/10 of the smallest feature dimension for all samples to ensure simulation accuracy. Additionally, a mass scaling technique was employed to obtain results with a reasonable computation time.

We started with simulations of two hydrogel layers with the same aspect ratio as the experiments ($R_0/H = 4.8$): one without torsion ($\alpha = 0°$) and the other with torsion ($\alpha = 40°$). The nominal stress–stretch curves from the simulations are shown in Figs. 4a and 4c. Consistent with the experimental results (Fig. 3), the hydrogel layer without torsion experiences a non-monotonic stress–stretch relationship with a critical stretch of $\lambda_c = 1.5$ at the initiation of the fingering instability (Figs. 4a and 4b). In contrast, the hydrogel layer with torsion displays a monotonic stress–stretch relationship (Figs. 4c and 4d) with the same critical stretch of $\lambda_c = 1.5$ at the initiation of the fingering instability (Fig. 4d), validating the role of torsion in stabilizing the fingering process. Additionally, the simulation shows a negative stress at $\lambda = 1$ for the hydrogel layer with torsion (Fig. 4c), consistent with the Poynting effect observed in the experiments (Fig. 3c). Similar to the experimental observations, our simulations demonstrate that as the hydrogel layer undergoes large deformations, some developing fingers continue to grow while others are suppressed.

According to existing studies (Lin et al., 2016, 2017), confined elastic layers subjected to tension can exhibit either fringe or fingering instabilities, depending on the location where the instabilities initiate. This study focuses on fingering instabilities, but a brief discussion of fringe instabilities in samples with low aspect ratios is given in Appendix C. It is shown that torsion can affect the location along the sample's height where the fringe instability initiates, and that torsion affects the aspect ratio at which the fringe-to-fingering transition occurs. Torsion is shown to have no effect on the number of undulations in samples with either fringe or fingering instabilities.

5. Theoretical analysis

The theoretical analysis developed next follows a similar approach to that in Lin et al. (2016). We restrict the analysis to the response of incompressible hyperelastic samples up to the onset of the instability. We consider only axially symmetric deformations, which is a valid approximation up to the first appearance of the undulating patterns, and we assume that the horizontal planes in the samples remain horizontal upon deformation. As shown by Lin et al. (2016), this approach indeed reveals emergence of a peak load and a non-monotonic stress–stretch curve for rectangular samples with width-to-height aspect ratios above 5.1, without the application of torsion. Here, we extend the formulation to cylindrical samples and account for the transverse motion induced by rotation of the top plate.

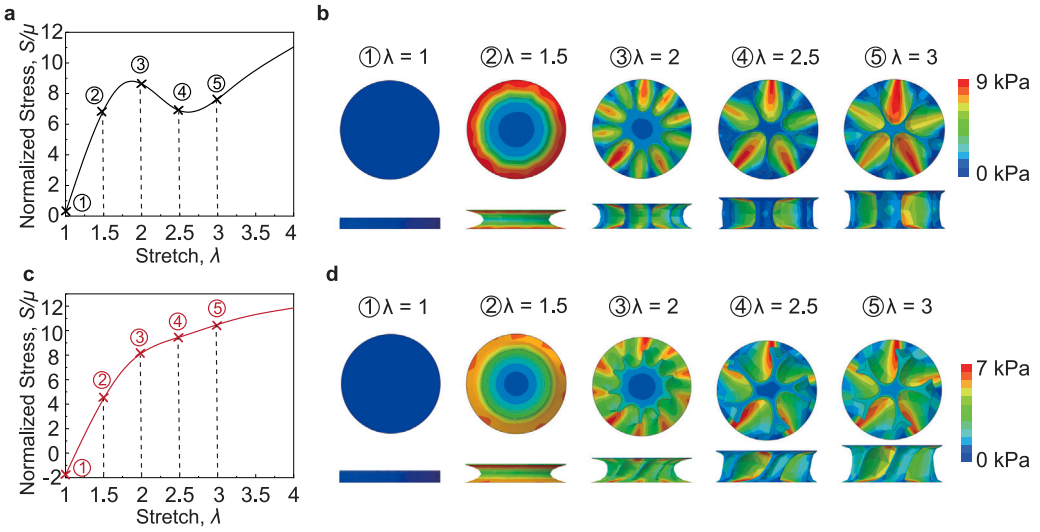


Fig. 4. Comparison between simulated mechanical responses of hydrogel layers ($R_0/H = 4.8$) with and without torsion. (a) Normalized nominal stress S/μ versus stretch λ of the hydrogel layer without torsion ($\alpha = 0°$) under tension. (b) Top and side views of the initiation and development of fingering patterns in the hydrogel layer without torsion ($\alpha = 0°$) at various stretches. (c) Normalized nominal stress S/μ versus stretch λ of the hydrogel layer with torsion ($\alpha = 40°$) under tension. (d) Top and side views of the initiation and development of fingering patterns in the hydrogel layer with torsion ($\alpha = 40°$) at various stretches. The color scales in (b) and (d) refer to von Mises stress.

5.1. Boundary conditions and kinematic assumptions

Returning to the problem setting in Fig. 1 with the reference coordinates (R, Θ, Z) illustrated in Eq. (1) with the origin in the center of the cylinder, we define the coordinates in the deformed configuration as the corresponding set (r, θ, z). The perfect bonding between the glass plates and the samples implies the displacement boundary conditions

$$\begin{aligned} Z = +H/2: &\qquad r = R, \qquad \theta = \alpha, \qquad z = +h/2, \\ Z = -H/2: &\qquad r = R, \qquad \theta = 0, \qquad z = -h/2, \end{aligned} \tag{2}$$

on the top and bottom surfaces, respectively. The lateral surface is considered to be stress-free.

Next, we employ two additional simplifying kinematic assumptions that are supported by observations from both the experiments and the numerical simulations. First, we assume that radial lines in the horizontal planes remain radial upon deformation. When this assumption is combined with the assumption that horizontal planes remain horizontal, we can simplify the equations so z is only a function of Z, and the deformed radial coordinate r is independent of Θ. Second, the rotation angle of the horizontal planes is assumed to vary linearly along the Z coordinate. Considering these assumptions along with the boundary conditions in Eq. (2), the deformed coordinates can be expressed as follows

$$r = g(R, Z), \qquad \theta = \Theta + \alpha\left(\frac{1}{2} + \frac{Z}{H}\right), \qquad z = f(Z), \tag{3}$$

where f and g are arbitrary functions, and the deformation gradient can be written as

$$\mathbf{F} = \begin{bmatrix} \frac{\partial g}{\partial R} & 0 & \frac{\partial g}{\partial Z} \\ 0 & \frac{g}{R} & g\frac{\alpha}{H} \\ 0 & 0 & f' \end{bmatrix} \tag{4}$$

with the superimposed prime denoting differentiation, such that $f' = df/dZ$.

Recalling that the incompressibility constraint implies that $\det(\mathbf{F}) = 1$, we obtain a relationship that can be directly integrated after separation of variables to write

$$\frac{\partial g}{\partial R}\frac{g}{R}f' = 1 \qquad \rightarrow \qquad g = \frac{R}{\sqrt{f'}} \tag{5}$$

where we have applied the condition that $r = g(0, Z) = 0$ from Eq. (2) to eliminate the integration constant.

This relationship allows us to eliminate g and express the deformation gradient purely as a function of f, Z, and R, as

$$\mathbf{F} = \begin{bmatrix} \frac{1}{\sqrt{\frac{df}{dZ}}} & 0 & \frac{-R}{2(\frac{df}{dZ})^{\frac{3}{2}}}\frac{d^2f}{dZ^2} \\ 0 & \frac{1}{\sqrt{\frac{df}{dZ}}} & \frac{R}{\sqrt{\frac{df}{dZ}}}\frac{\alpha}{H} \\ 0 & 0 & \frac{\partial f}{\partial Z} \end{bmatrix} \tag{6}$$

With the above restrictions on the deformation field, and with the above dependence of g on R and f', the boundary conditions in Eq. (2) reduce to

$$\begin{aligned} Z = +H/2: \quad & f = +h/2, \quad f' = 1, \\ Z = -H/2: \quad & f = -h/2, \quad f' = 1, \end{aligned} \tag{7}$$

5.2. Constitutive response and governing equation

We represent the material response using the neo-Hookean elastic strain energy density, which can be written in the form

$$\Psi = \frac{\mu}{2}\left(\mathrm{tr}(\mathbf{F}\mathbf{F}^{\mathrm{T}}) - 3\right) \tag{8}$$

The total elastic energy in the material system can thus be obtained by integration over the volume of the sample

$$\mathcal{E} = \iiint_V \Psi \mathrm{d}V = \frac{\mu}{2}\int_0^{2\pi}\int_0^{R_0}\int_{-\frac{H}{2}}^{\frac{H}{2}} \left\{ \frac{1}{f'}\left[2 + \left(\frac{R}{2}\frac{f''}{f'}\right)^2 + \left(\frac{R\alpha}{H}\right)^2\right] + (f')^2 - 3 \right\} R\mathrm{d}Z\mathrm{d}R\mathrm{d}\Theta \tag{9}$$

where we have substituted the deformation gradient from Eq. (4), along with the relation from Eq. (5).

Performing the above integration with respect to Θ and R, and transforming to the dimensionless coordinate $\zeta = Z/H$, with the dimensionless function $\hat{f}(\zeta) = f(\zeta H)/H$, reads

$$\mathcal{E} = \pi\mu R_0^2 \int_{-1/2}^{1/2} \mathcal{L}(\hat{f}', \hat{f}'')\mathrm{d}\zeta \quad \text{where} \quad \mathcal{L} = \frac{1}{\hat{f}'}\left\{1 + \left(\frac{R_0}{H}\right)^2\left[\left(\frac{\hat{f}''}{4\hat{f}'}\right)^2 + \left(\frac{\alpha}{2}\right)^2\right]\right\} + \frac{1}{2}((\hat{f}')^2 - 3) \tag{10}$$

which leaves us with an energy functional that depends on a single unknown function and its derivatives.

Within the confines of our kinematic assumptions, an equilibrium solution would minimize the total elastic energy in the system. To find the function $\hat{f}$ that minimizes the energy, we use the method of variations. The resulting differential equation takes the general form

$$\frac{\mathrm{d}}{\mathrm{d}\zeta}\left(\frac{\partial \mathcal{L}}{\partial \hat{f}'}\right) = \frac{\mathrm{d}^2}{\mathrm{d}\zeta^2}\left(\frac{\partial \mathcal{L}}{\partial \hat{f}''}\right) \tag{11}$$

Substituting $\mathcal{L}$ from Eq. (10) in the above formula, we obtain after some simplification the fourth order nonlinear ordinary differential equation

$$8(\hat{f}')^5\hat{f}'' + 16(\hat{f}')^2\hat{f}'' + \left(\frac{R_0}{H}\right)^2\left(6\hat{f}'\hat{f}''\hat{f}''' + 4\alpha^2(\hat{f}')^2\hat{f}'' - (\hat{f}')^2\hat{f}'''' - 6(\hat{f}'')^3\right) = 0 \tag{12}$$

with the condition $\hat{f}' \neq 0$. This governing equation can be solved for $f(z) = H\hat{f}(z/H)$ using the boundary conditions in Eq. (7) to determine the deformation of a sample with a given aspect ratio R_0/H, subjected to torsion angle α and stretch $\lambda = h/H$. In this work, we perform the integration using the MATLAB boundary value problem solver BVP5C.

5.3. Force–displacement relationship and meniscus shape

Once the function f is obtained for a given set $(h, R_0/H, \alpha)$, the total elastic energy in the system $\mathcal{E} = \mathcal{E}(h, R_0/H, \alpha)$ is found by evaluating the integral in Eq. (10). We can then directly calculate the applied normal force and the corresponding nominal stress using the same methodology as in Lin et al. (2016), to write

$$F(h, R_0/H, \alpha) = \frac{\partial \mathcal{E}}{\partial h} \qquad \text{where} \qquad S = \frac{F}{\pi R_0^2} \tag{13}$$

Another key result from the numerical integration is the shape of the meniscus. As the sample undergoes axial extension, the side of the sample curves. The shape of the meniscus can be found directly from Eq. (5) as $r_0 = R_0/\sqrt{f'(Z)}$. The effect of torsion on the meniscus shape is discussed further in Appendix D.

In the next section we will show the results of this model and their comparison to the experimental and numerical results.

6. Results and discussion

In this section, we use the theory and experiments to investigate the normalized nominal stress (S/μ) versus stretch (λ) curves of confined elastic layers with various aspect ratios R_0/H under tension and torsion angle α. We first focus on the stress–stretch curves of elastic layers with different aspect ratios under tension without torsion ($\alpha = 0°$). As shown in Fig. 5b, our theory predicts a monotonic stress–stretch relationship for elastic layers with small aspect ratios (e.g. $R_0/H = 4$). As the aspect ratio increases, the nominal stress increases due to the volumetric confinement applied on the incompressible elastic layer (Lin et al., 2016). When the aspect ratio reaches a critical threshold of 4.8, the stress–stretch relationship starts to exhibit a peak, resulting in a non-monotonic stress–strain relationship. As the aspect ratio further increases, the peak stress increases, while the stretch corresponding to the peak stress decreases. To validate our theoretical calculations, we measure the nominal stress versus stretch curves of confined hydrogel layers with the same aspect ratios under tension without torsion. The nominal stress is normalized by the hydrogel layer's modulus.

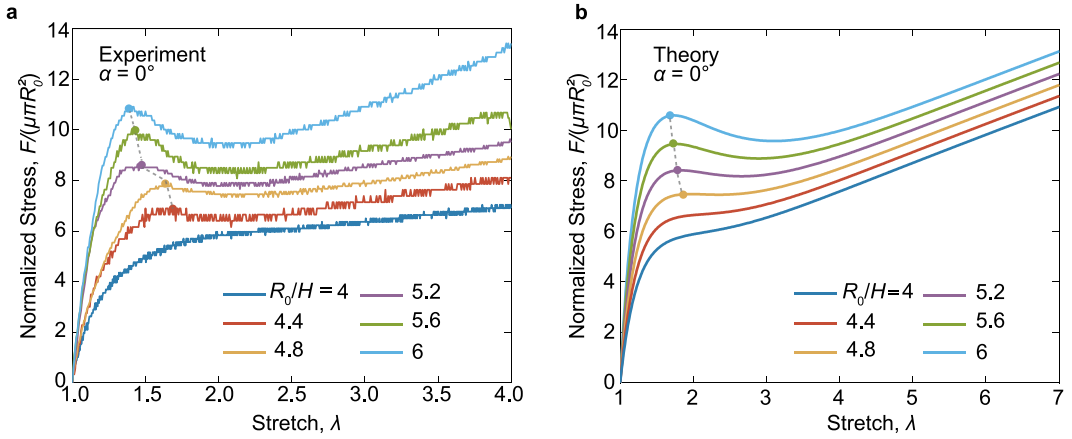


Fig. 5. Normalized nominal stress versus stretch curves from (a) experiment and (b) theory with no applied torsion, for samples with aspect ratios from 4 to 6.

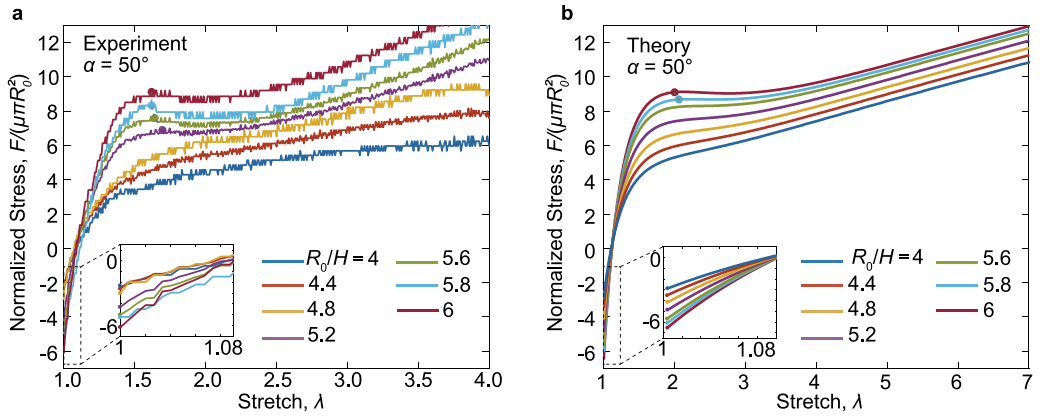


Fig. 6. Normalized nominal stress versus stretch curves from (a) experiment and (b) theory with applied torsion angle $\alpha = 50°$, for samples with aspect ratios from 4 to 6.

As shown in Fig. 5a, a striking agreement is observed between our theoretical calculations and the experimental measurements. The minimum aspect ratio at which a nonmonotonic curve appears in the theory is 4.8 compared to the value of $\sim$ 4.4 from the experiment.

We next focus on the stress–stretch curves of elastic layers with different aspect ratios under tension with torsion ($\alpha = 50°$). As shown in Fig. 6, in contrast to the elastic layers without torsion ($\alpha = 0°$) in Fig. 5, our theory and experiments produce negative stress at $\lambda = 1$, capturing the Poynting effect. As the aspect ratio increases, the negative stress at $\lambda = 1$ increases accordingly, suggesting that the Poynting effect becomes more pronounced in elastic layers with larger aspect ratios. Similar to the elastic layers without torsion ($\alpha = 0°$), the stress–stretch curve exhibits a monotonic-to-nonmonotonic transition as the aspect ratio reaches a critical threshold. However, the critical threshold increases to $\sim$ 5.2 in the experimental results and 5.8 in the theoretical results, indicating the role of torsion in tuning the stress–stretch curve monotonicity of these confined elastic layers. As shown in Fig. 6b, our theoretical trends agree with the experimental measurements.

Next, we examine the stress–stretch curves of elastic layers under tension with a fixed aspect ratio $R_0/H = 4.8$ but subjected to different torsion angles. As shown in Fig. 7, the elastic layer under tension without torsion ($\alpha = 0°$) exhibits a nonmonotonic stress–stretch relationship. As the torsion angle increases, the stress decreases, with a pronounced Poynting effect that manifests as negative stress at $\lambda = 1$. The increase of torsion angle suppresses the peak in the stress–stretch curve and causes the curve to switch from nonmonotonic to monotonic, indicating the role of torsion in modulating elastic instabilities. As shown in Fig. 7b, our theoretical predictions match the experimental measurements, with a slight difference: the transition from monotonic to nonmonotonic occurs between 0° and 20° for the theory, and between 20° and 40° for the experiment.

7. A phase diagram for instabilities

As the applied stretch on the confined elastic layers reaches a critical value, a mechanical instability sets in. Our theoretical calculations and experimental measurements in Section 6 show that the torsion angle α plays a critical role in tuning the

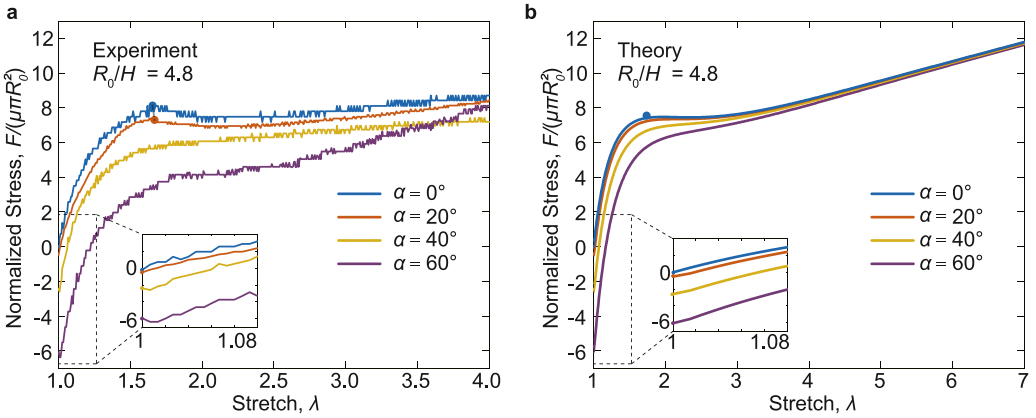


Fig. 7. Normalized nominal stress versus stretch curves from (a) experiment and (b) theory with aspect ratio $R_0/H = 4.8$ and varying torsion angles from 0° to 60°.

monotonicity of the stress–stretch curves. Additionally, while the selection of the instability mode is predominantly governed by the aspect ratio R_0/H of the elastic layer, our simulation results in Appendix C suggest that the application of torsion can tune the location where the instability initiates, thereby modulating between fringe and fingering instabilities in confined elastic layers. Therefore, we construct a phase diagram in the plane of torsion angle α and aspect ratio R_0/H as a guideline to predict the mode of instability and the monotonicity of the stress–stretch curve in the confined elastic layers.

For elastic layers with small aspect ratios, the fringe instability occurs. Since fringe patterns are always associated with monotonic stress–stretch relationships, they are denoted as "stable". As the aspect ratio reaches a critical threshold $(R_0/H)_{\text{mode}}$, the fringe instability transitions to a fingering instability, indicated by the relocation of horizontal plane where instability initiates (see Appendix C). For example, for elastic layers without torsion ($\alpha = 0°$), the critical aspect ratio for the transition from fringe instability to fingering instability is 3.5 (Fig. 8). For an elastic layer with an aspect ratio slightly larger than this threshold, although the layer exhibits a fingering transition, it still shows a monotonic stress–stretch relationship, indicating its stable nature. As the aspect ratio further increases to the other critical threshold, $(R_0/H)_{\text{stability}}$ (e.g. 4.5 for an elastic layer with $\alpha = 0°$), the stress–stretch curve of the layer transitions from a monotonic to nonmonotonic relationship. Note that we distinguish here between the geometric instability and the performance of the cylinder as a component. Although in both cases the circumferential undulations (i.e. fingering) will emerge, a non-monotonic stress–stretch response implies that in a load-controlled setting there exists a critical force beyond which the cylinder will 'snap' to a new configuration. We refer to this as 'unstable fingering', while a monotonic transition is considered 'stable fingering'.

We next use theory and simulation to investigate the role of torsion in selecting the mode and stress–stretch curve monotonicity of the fringe and fingering patterns in confined elastic layers. As shown in Fig. 8, for elastic layers with small aspect ratios (e.g. $R_0/H = 1$), the mode is always fringe instability regardless of the torsion angle. For elastic layers with a moderate aspect ratio (e.g. $R_0/H = 3$), the mode shifts from fringe to stable fingering as the torsion angle increases. For elastic layers with a larger aspect ratio (e.g. $R_0/H = 6$), there is a transition from unstable to stable fingering as the torsion angle increases, demonstrating that the instability is gradually suppressed. For elastic layers with a very high aspect ratio (e.g. $R_0/H = 8$), the transition from unstable to stable status is not achieved until the torsion angle reaches 80°.

8. Conclusions

In this paper, we performed a systematic study on the impact of torsional loading on the appearance of instabilities in a confined elastic layer through combined experimental, simulation, and theoretical analysis. We constructed a phase diagram to quantitatively predict the mode of fringe and fingering patterns, characterized by the location where the undulation initiates, and the monotonicity of the stress–stretch curve. We demonstrate that applying torsion can tune between fringe and fingering modes in elastic layers with moderate aspect ratios. Additionally, torsion controls the monotonicity of the stress–stretch relationship in elastic layers with large aspect ratios. Our phase diagram delineates the mode of instabilities and the monotonicity of stress–stretch curves in the confined elastic layers as a function of torsion angle and cylinder aspect ratio.

This work not only provides mechanistic insights into the role of torsion in stabilizing the response of confined elastic layers, but also offers a valuable tool for designing soft yet tough adhesive systems capable of withstanding complex mechanical loads. Applying torsion to soft adhesives under tensile loads can suppress instabilities, transitioning from a non-monotonic to a monotonic stretch–stress relationship. This suppression reduces stress concentrations and minimizes crack initiation, significantly enhancing the adhesive's fracture resistance and durability. Finally, this work is not without limitations; while the experimental samples used in this work are well characterized by the neo-Hookean model, different materials that may be better characterized by different hyperelastic models may reveal additional phenomena that are not captured by the present analysis. Consequently, exploring these alternative models presents a promising avenue for future research.

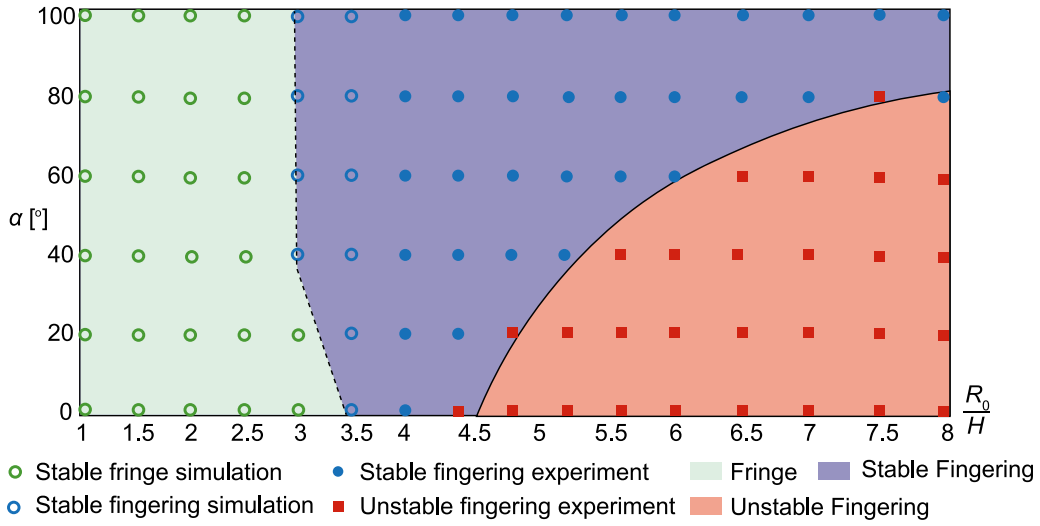


Fig. 8. Phase diagram in the plane of torsion angle α and aspect ratio R_0/H for predicting the mode of instability and monotonicity of the stress–stretch curve in confined elastic layers. Green hollow circles denote the occurrence of the fringe instability in simulations; blue hollow circles denote the occurrence of stable fingering patterns in simulations; blue solid circles denote the occurrence of stable fingering patterns in experiments; and red solid squares denote the occurrence of unstable fingering patterns in experiments. The black dashed line represents the critical aspect ratio $(R_0/H)_{\text{mode}}$ identified by the simulation, which defines the mode transition between fringe and fingering patterns. The black solid line represents the critical aspect ratio $(R_0/H)_{\text{stability}}$ identified by the theory, which defines the stability transition characterized by monotonic and non-monotonic stress–stretch relationships. The experimental results generally follow the stability boundary from the theory, with slight discrepancies due to theoretical assumptions and experimental errors.

CRediT authorship contribution statement

Tara K. Venkatadri: Writing – review & editing, Writing – original draft, Methodology, Investigation, Formal analysis, Data curation, Conceptualization. **Chuwei Ye:** Writing – review & editing, Writing – original draft, Methodology, Investigation, Formal analysis, Data curation. **Tal Cohen:** Writing – review & editing, Writing – original draft, Supervision, Methodology, Funding acquisition, Conceptualization. **Shaoting Lin:** Writing – review & editing, Writing – original draft, Supervision, Methodology, Investigation, Funding acquisition, Conceptualization.

Declaration of competing interest

The authors declare the following financial interests/personal relationships which may be considered as potential competing interests: Shaoting Lin reports financial support was provided by National Science Foundation. Tal Cohen reports financial support was provided by National Science Foundation. Tal Cohen reports financial support was provided by Office of Naval Research. Tara K. Venkatadri reports financial support was provided by Barry Goldwater Scholarship and Excellence in Education Foundation. If there are other authors, they declare that they have no known competing financial interests or personal relationships that could have appeared to influence the work reported in this paper.

Acknowledgments

T. C. acknowledges the partial support of our work through Office of Naval Research grant N000142312530, and the support from the National Science Foundation under award number CMMI 1942016. T. K. V. acknowledges the Barry Goldwater Scholarship and the support of the MIT Undergraduate Research Opportunities Program. S. L. acknowledges the partial support of our work through National Science Foundation under award number CMMI 2338747.

Appendix A. Shear modulus characterization of the hydrogel samples

A pure shear test was conducted to obtain the shear modulus μ of the hydrogel samples. As shown in Fig. A.1, the experimental result curve was fitted to a neo-Hookean model. The shear modulus of the hydrogel material was found to be approximately 0.24 kPa.

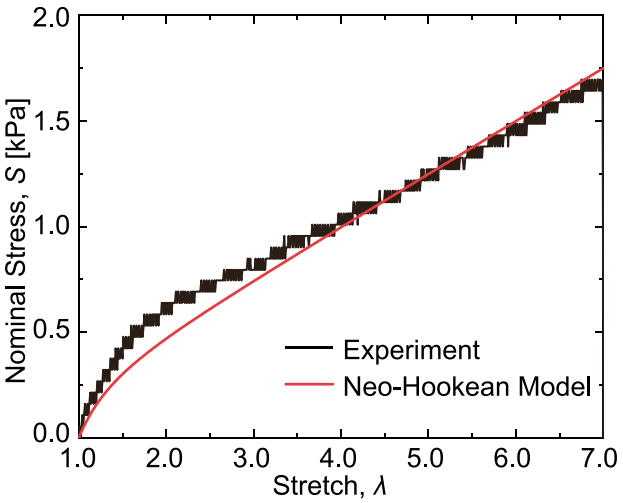


Fig. A.1. Pure shear experimental result and theoretical fitting curve based on neo-Hookean model to obtain the shear modulus of the sample.

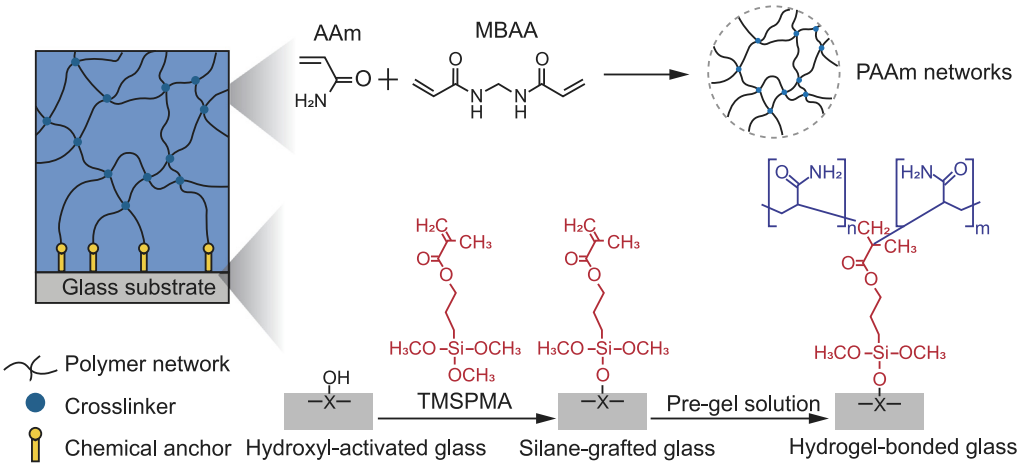


Fig. B.1. Schematic of the synthesis chemistry for fabricating the hydrogel layers and the surface chemistry for bonding the hydrogel layers to the glass substrates.

Appendix B. Fabrication of hydrogel samples

This appendix describes the process to produce the hydrogel samples discussed in the main text. We chose poly(acrylamide) hydrogel (PAAm) as a model hyperelastic solid due to its negligible mechanical hysteresis and minimal rate dependence. To make a PAAm hydrogel sample, we first prepared a 10 mL aqueous precursor solution by mixing 0.3 g acrylamide (AAm, Sigma-Aldrich A8887) as the monomer, 0.6 mg N,N-methylenebisacrylamide (MBAA, Sigma-Aldrich 146072) as the crosslinker, 100 μL 10 wt% ammonium persulfate (APS, Sigma-Aldrich 248614) as the thermal initiator, 10 μL N,N,N',N'-tetramethylethylene-diamine (TEMED, Sigma-Aldrich T7024-50M) as the accelerator, and 50 mg sodium alginate (Sigma-Aldrich A2033) as the viscosity booster. After vigorous mixing, the precursor solution was degassed in a vacuum chamber. To achieve robust bonding between the hydrogel and the glass substrates, we treated the glass substrates with 3-(trimethoxysilyl) propyl methacrylate (TMSPMA, Sigma-Aldrich 104884) saline (Fig. B.1). In each 200 mL aqueous saline solution, we added 60 μL acetic acid (Sigma A6283) and 800 μL TMSPMA, stirring for 3 h. Thereafter, the glass slides were soaked in the silane for 2 h, followed by drying with nitrogen flow. This treatment ensured that the cured hydrogels bonded firmly to the glass slides without interfacial detachment.

Appendix C. Numerical simulations for fringe and fingering instabilities

This section describes the finite element models of fringe instabilities in samples with low aspect ratios, and contrasts them to the fingering instabilities for higher aspect ratios. The fringe instability initiates at the fringe portion of the elastic layer, while the fingering instability initiates at the middle portion of the elastic layer. One advantage of the simulation is its ability to identify

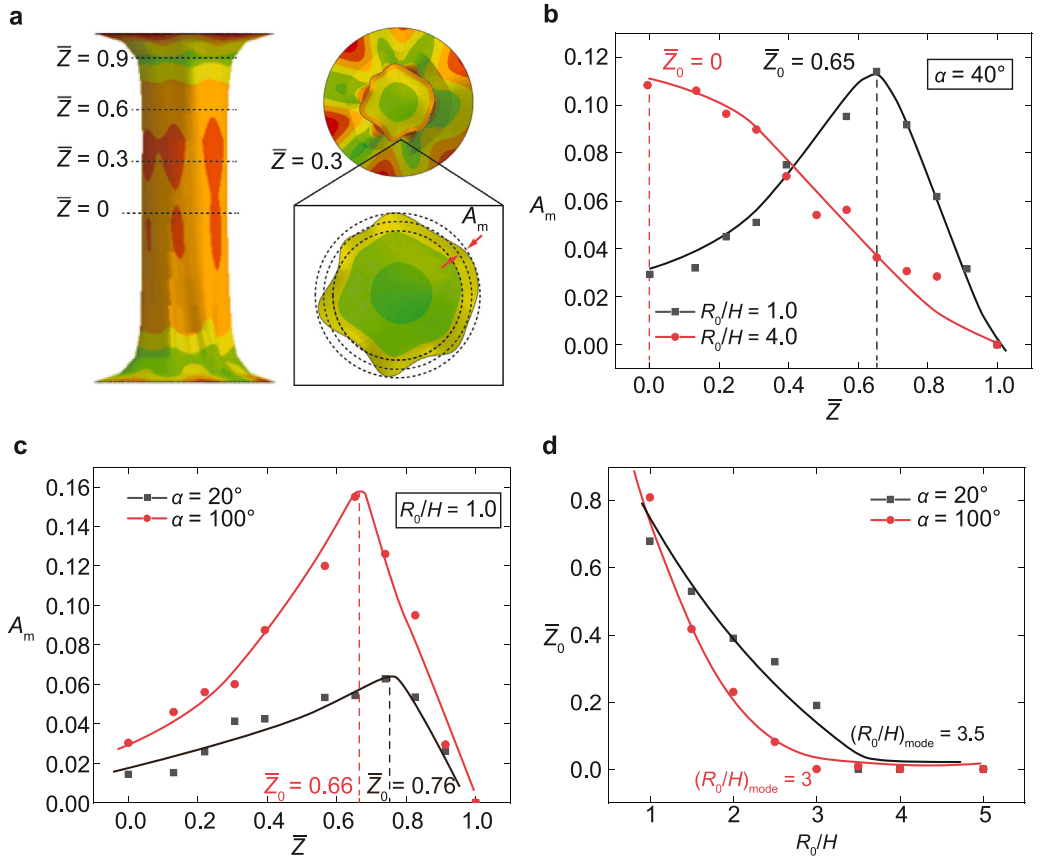


Fig. C.1. Effects of aspect ratio and torsion angle on the mode of elastic instabilities in simulated elastic layers. (a) Extraction of cross-sectional area at various vertical locations $\overline{Z}$ of the elastic layer with $R_0/H = 1$ at the onset of instability in the simulation. By analyzing the undulating contour shape of each cross-sectional area, we identify the corresponding amplitude A_m at different vertical locations $\overline{Z}$. (b) Cross-sectional amplitude A_m as a function of vertical locations $\overline{Z}$ of the elastic layers with different aspect ratios at the onset of instability, subjected to the same torsion angle $\alpha = 40°$. The amplitude peaks at $\overline{Z}_0 = 0.66$ for the layer with $R_0/H = 1$ and at $\overline{Z}_0 = 0$ for the layer with $R_0/H = 4$. (c) Cross-sectional amplitude A_m as a function of vertical locations $\overline{Z}$ of the elastic layer with $R_0/H = 1$ at the onset of instability, subjected to different torsion angles. The amplitude peaks at $\overline{Z}_0 = 0.76$ when subjected to torsion $\alpha = 20°$ and at $\overline{Z}_0 = 0.66$ when subjected to torsion $\alpha = 100°$. (d) The location $\overline{Z}_0$ where instability initiates as a function of the elastic layer's aspect ratio R_0/H under different torsion angles. The critical aspect ratios corresponding to the transition between fingering and fringe instabilities are $(R_0/H)_{mode} = 3.5$ for elastic layers subjected to torsion angle $\alpha = 20°$ and $(R_0/H)_{mode} = 3$ for elastic layers subjected to torsion angle $\alpha = 100°$.

the mode of elastic instabilities by locating the highest amplitude of the undulation at the onset of instability. Here, we take the vertical location that yields the highest undulation amplitude $\overline{Z}_0$ as the location where the instability initiates in the simulation. As shown in Fig. C.1a, we extract the cross-sectional area at various vertical locations $\overline{Z}$ of the elastic layer at the onset of instability. By analyzing the undulating contour shape of each cross-sectional area, we identify the corresponding amplitude A_m at different vertical locations $\overline{Z}$. We first plot the amplitude A_m as a function of vertical locations $\overline{Z}$ for elastic layers with different aspect ratios at a fixed torsion angle $\alpha = 40°$. As shown in Fig. C.1b, for the elastic layer with large aspect ratio (i.e. $R_0/H = 4$), the highest amplitude of the cross-sectional area is located at the middle portion of the layer, $\overline{Z}_0 = 0$, suggesting its mode to be fingering instability. In contrast, for the elastic layer with small aspect ratio (i.e., $R_0/H = 1$), the highest amplitude of the cross-sectional area is located at the fringe portion of the layer, $\overline{Z}_0 = 0.65$, suggesting its mode to be fringe instability. We also plot the amplitude A_m as a function of vertical locations $\overline{Z}$ for the elastic layer with aspect ratio $R_0/H = 1$ under different torsion angles. As shown in Fig. C.1c, the amplitude A_m peaks at $\overline{Z}_0 = 0.76$ when the elastic layer is subjected to torsion angle $\alpha = 20°$, and at $\overline{Z}_0 = 0.66$ when subjected to torsion angle $\alpha = 100°$. This indicates the role of torsion in tuning the initiation location of fringe instabilities. We further plot the initiation location of instabilities $\overline{Z}_0$ as a function of elastic layers' aspect ratio R_0/H. The elastic layer initiates undulations at the layers' fringe portions (i.e. $\overline{Z}_0 > 0$), exhibiting fringe instabilities, for layers with small aspect ratios, while initiating undulations at the layers' middle portions (i.e. $\overline{Z}_0 = 0$), exhibiting fingering instabilities, for layers with large aspect ratios. There exhibits a critical aspect ratio $(R_0/H)_{mode}$, which defines the transition between fringe and fingering instabilities. As summarized in Fig. C.1d, the presence of torsion does not alter the trend of transition from fringe instability to fingering instability as the aspect ratio increases. However, it decreases the critical aspect ratio $(R_0/H)_{mode}$, suggesting the role of torsion in tuning the mode of instabilities in confined elastic layers.

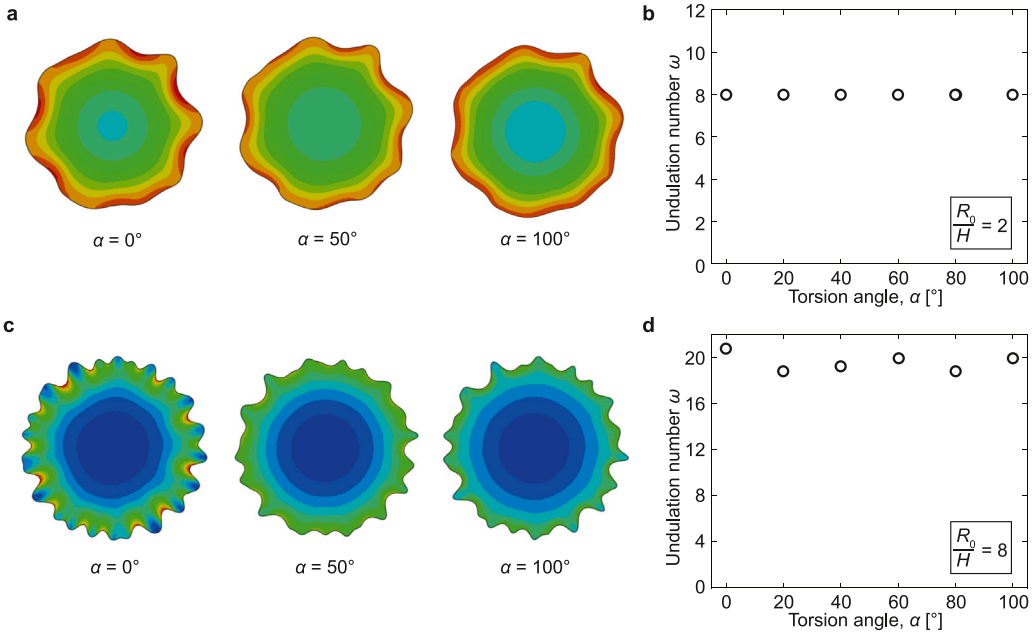


Fig. C.2. Effects of torsion angle on the undulation number of elastic instabilities in simulated elastic layers. (a) Cross-sectional area at the horizontal plane $\overline{Z}_0$ where instability initiates in elastic layers with aspect ratio $R_0/H = 2$ under various torsion angles ($\alpha = 0, 50, 100°$). (b) Undulation number ω versus torsion angle α in elastic layers with an aspect ratio $R_0/H = 2$. (c) Cross-sectional area at the horizontal plane $\overline{Z}_0$ where instability initiates in elastic layers with an aspect ratio $R_0/H = 8$ under various torsion angles ($\alpha = 0, 50, 100°$). (d) Undulation number ω versus torsion angle α in elastic layers with aspect ratio $R_0/H = 8$.

We further use simulations to investigate the role of torsion on the undulation number of instabilities in confined elastic layers — in contrast to the experiments, the simulations show a more uniform initiation and development of fingering instabilities, allowing for a more precise quantification of the undulation number. We specifically focus on layers with aspect ratio $R_0/H = 2$ (Figs. C.2a and C.2b) and $R_0/H = 8$ (Figs. C.2c and C.2d). As shown in Fig. C.2b, the elastic layers with an aspect ratio $R_0/H = 2$ exhibit the same undulation number of 8 under different torsion angles ranging from 0° to 100°. Similarly, the elastic layers with an aspect ratio $R_0/H = 8$ also exhibit torsion-independent undulation numbers around 20 (Fig. C.2d), indicating that the presence of torsion does not impact the undulation number.

Appendix D. Meniscus profile

In addition to the main results of the effect of torsion on the monotonicity of the force–displacement curve, we also examined the effect of torsion on the meniscus, the curved side profile of the cylindrical sample, when elongated to a given stretch ratio λ. Since the experiments did not yield any obvious changes in the meniscus shape for cases with and without torsion, we present results from the theory and FEA. A representative plot of the meniscus is shown in Fig. D.1, an aspect ratio $R_0/H = 1.25$, and an axial stretch $\lambda = 2$. The meniscus shape is plotted on the horizontal axis, and the deformed (nondimensional) height coordinate z/H is plotted on the vertical axis. The main figure is rescaled to demonstrate the slight differences between the meniscus shapes with and without torsion, while an inset figure is drawn to scale to highlight the similarity of these curves (which concurs with the lack of obvious meniscus changes in the experimental results). Solid lines denote the results from the theory, while individual dots represent data points from the simulation (which adhere well to the theory results). As shown in Fig. D.1, the meniscus shape is relatively resistant to change. Even if the torsion angle drastically increases to 100°, the meniscus shape still tracks relatively well with the curve obtained with no applied torsion. Therefore, we conclude that the shape of the meniscus depends only slightly on the torsion angle α.

Data availability

Data will be made available on request.

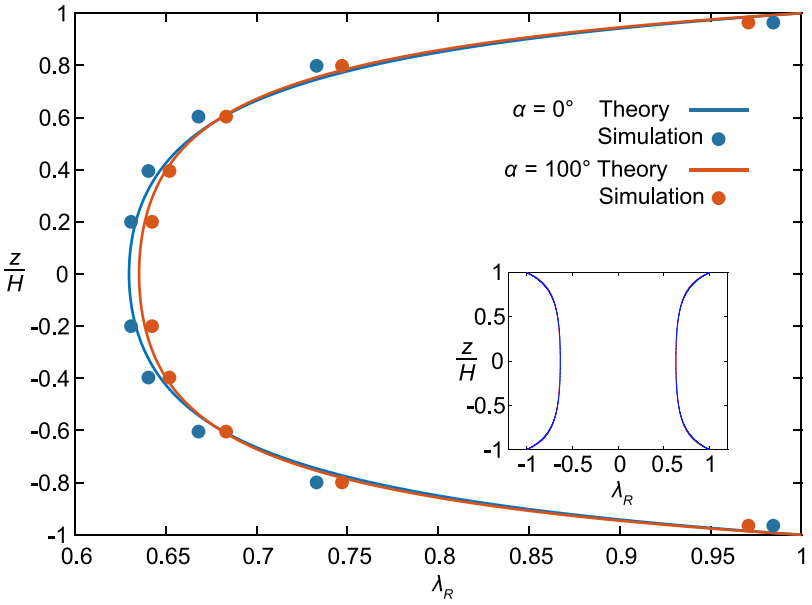


Fig. D.1. Meniscus profile in the plot of z/H versus $\lambda_R = r/R$ with $\alpha = 0°$ and $\alpha = 100°$, aspect ratio $R_0/H = 1.25$, and axial stretch ratio $\lambda = 2$. The curved lines represent the theoretical results, which match well with the FEA results (depicted as dots). In the main figure, the x-axis has been rescaled to highlight the slight differences between the meniscus shapes with and without rotation. The inset figure shows the analytical results of the meniscus shape for both sides of the sample with the same α, λ, and R_0/H values as the main figure, with the axes scaled equally to demonstrate the similarity of the meniscus shapes with and without torsion when drawn to scale.

References

Benjamin, M., Toumi, H., Ralphs, J.R., Bydder, G., Best, T., Milz, S., 2006. Where tendons and ligaments meet bone: attachment sites ('entheses') in relation to exercise and/or mechanical load. J. Anat. 208 (4), 471–490.

Biggins, J.S., Saintyves, B., Wei, Z., Bouchaud, E., Mahadevan, L., 2013. Digital instability of a confined elastic meniscus. Proc. Natl. Acad. Sci. 110 (31), 12545–12548.

Bovone, G., Dudaryeva, O.Y., Marco-Dufort, B., Tibbitt, M.W., 2021. Engineering hydrogel adhesion for biomedical applications via chemical design of the junction. ACS Biomater. Sci. Eng. 7 (9), 4048–4076.

Chakrabarti, A., Chaudhury, M.K., 2013. Direct measurement of the surface tension of a soft elastic hydrogel: exploration of elastocapillary instability in adhesion. Langmuir 29 (23), 6926–6935.

Chateauminois, A., Fretigny, C., Olanier, L., 2010. Friction and shear fracture of an adhesive contact under torsion. Phys. Rev. E 81 (2), 026106.

Chaudhury, M.K., Chakrabarti, A., Ghatak, A., 2015. Adhesion-induced instabilities and pattern formation in thin films of elastomers and gels. Eur. Phys. J. E 38, 1–26.

Ciarletta, P., Destrade, M., 2014. Torsion instability of soft solid cylinders. IMA J. Appl. Math. 79 (5), 804–819.

Craik, R.J., Osipov, A.G., 1995. Structural isolation of walls using elastic interlayers. Appl. Acoust. 46 (3), 233–249.

Cui, C., Wu, T., Chen, X., Liu, Y., Li, Y., Xu, Z., Fan, C., Liu, W., 2020. A janus hydrogel wet adhesive for internal tissue repair and anti-postoperative adhesion. Adv. Funct. Mater. 30 (49), 2005689.

Desmond, K.W., Zacchia, N.A., Waite, J.H., Valentine, M.T., 2015. Dynamics of mussel plaque detachment. Soft Matter 11 (34), 6832–6839.

Feng, H., Ma, Y., Zhang, Z., Yang, S., Ma, Z., Zhang, Y., Ma, S., Yu, B., Cai, M., Pei, X., et al., 2022. Reversing hydrogel adhesion property via firmly anchoring thin adhesive coatings. Adv. Funct. Mater. 32 (15), 2111278.

Gent, A., Hua, K.-C., 2004. Torsional instability of stretched rubber cylinders. Int. J. Non-Linear Mech. 39 (3), 483–489.

Her, S.-C., Chan, C.-F., 2019. Interfacial stress analysis of adhesively bonded lap joint. Materials 12 (15), 2403.

Hu, Y., Suo, Z., 2012. Viscoelasticity and poroelasticity in elastomeric gels. Acta Mech. Solida Sin. 25 (5), 441–458.

Kaniewska, K., Karbarz, M., Katz, E., 2020. Nanocomposite hydrogel films and coatings–features and applications. Appl. Mater. Today 20, 100776.

Kanner, L.M., Horgan, C.O., 2008. On extension and torsion of strain-stiffening rubber-like elastic circular cylinders. J. Elasticity 93, 39–61.

Khutoryanskaya, O.V., Potgieter, M., Khutoryanskiy, V.V., 2010. Multilayered hydrogel coatings covalently-linked to glass surfaces showing a potential to mimic mucosal tissues. Soft Matter 6 (3), 551–557.

Lin, S., Cohen, T., Zhang, T., Yuk, H., Abeyaratne, R., Zhao, X., 2016. Fringe instability in constrained soft elastic layers. Soft Matter 12 (43), 8899–8906.

Lin, S., Mao, Y., Radovitzky, R., Zhao, X., 2017. Instabilities in confined elastic layers under tension: Fringe, fingering and cavitation. J. Mech. Phys. Solids 106, 229–256.

Liu, J., Qu, S., Suo, Z., Yang, W., 2021. Functional hydrogel coatings. Natl. Sci. Rev. 8 (2), nwaa254.

Osipov, A., Vermeir, G., 1996. Sound transmission in buildings with elastic layers at joints. Appl. Acoust. 49 (2), 141–162.

Small, G., Berjamin, H., Balbi, V., 2024. Poynting effect in fluid-saturated poroelastic soft materials in torsion. Int. J. Non-Linear Mech. 159, 104601.

Söntjens, S.H., Nettles, D.L., Carnahan, M.A., Setton, L.A., Grinstaff, M.W., 2006. Biodendrimer-based hydrogel scaffolds for cartilage tissue repair. Biomacromolecules 7 (1), 310–316.

Sun, Y., Guo, S., Walker, G.C., Kavanagh, C.J., Swain, G.W., 2004. Surface elastic modulus of barnacle adhesive and release characteristics from silicone surfaces. Biofouling 20 (6), 279–289.

Vaccaro, E., Waite, J.H., 2001. Yield and post-yield behavior of mussel byssal thread: a self-healing biomolecular material. Biomacromolecules 2 (3), 906–911.

Venkatadri, T.K., Henzel, T., Cohen, T., 2023. Torsion-induced stick-slip phenomena in the delamination of soft adhesives. Soft Matter 19 (13), 2319–2329.

Waite, J.H., Andersen, N.H., Jewhurst, S., Sun, C., 2005. Mussel adhesion: finding the tricks worth mimicking. J. Adhes. 81 (3–4), 297–317.
Wang, Y., Kankala, R.K., Ou, C., Chen, A., Yang, Z., 2022. Advances in hydrogel-based vascularized tissues for tissue repair and drug screening. Bioact. Mater. 9, 198–220.
Wang, M., Kornfield, J.A., 2012. Measuring shear strength of soft-tissue adhesives. J. Biomed. Mater. Res. Part B: Appl. Biomater. 100 (3), 618–623.
Wang, S.-Q., Ravindranath, S., Boukany, P., 2011. Homogeneous shear, wall slip, and shear banding of entangled polymeric liquids in simple-shear rheometry: A roadmap of nonlinear rheology. Macromolecules 44 (2), 183–190.
Ye, C., Lin, S., 2024. A mechano-diffusion characterization platform for probing strain-programmable nanoparticle diffusion in hydrogels. MRS Commun. 1–8.
Yuk, H., Zhang, T., Lin, S., Parada, G.A., Zhao, X., 2016. Tough bonding of hydrogels to diverse non-porous surfaces. Nat. Mater. 15 (2), 190–196.